J Mater Sci (2006) 41:4394–4404
DOI 10.1007/s10853-006-0093-9

Quantitative EFTEM measurement of the composition of embedded particles

S. Lozano-Perez · J. M. Titchmarsh · M. L. Jenkins

Received: 30 November 2005 / Accepted: 8 February 2006 / Published online: 28 June 2006

Abstract The optimisation of parameters is investigated for the compositional analysis of nanometre-sized particles embedded in a matrix by energy-filtered transmission electron microscopy. The specific example of Cu-rich particles in a Fe matrix is used both to model and to explore the experimental limits of detection and characterisation. Modelling of alternative procedures for background extrapolation as a function of the number of pre-edge windows confirmed that greater accuracy in a fixed analysis time is achieved by using more than two pre-edge windows. Further modelling investigated the effects of noise, drift and instrumental blurring of images on the accuracy of particle size and composition measurements. Correction factors were generated for ranges of these artefact amplitudes. The corrections were then applied to experimental data and shown to be both realistic and effective. Determination of particle radius below 1 nm was demonstrated.

Introduction

The detection and characterisation of Cu-rich clusters and particles induced by neutron irradiation in ferritic steel components has important consequences for the safety of nuclear reactor pressure vessel integrity [1–3]. Such individual clusters are typically ~1 nm in size and can usually only be directly imaged by Position Sensitive Atom Probe analysis (POSAP) [4–6]. The particles can also be characterised by bulk material measurements using Small Angle Neutron Scattering, Positron Annihilation and Electrical Resistivity [4, 7]. The various techniques sometimes provide conflicting information concerning the size distribution, number density and composition of particles that detract from estimates of component lifetime required by nuclear regulatory authorities [8]. Recently, advances in Energy Dispersive X-ray Analysis [9, 10] and Electron Energy-Loss methods in the transmission electron microscope (TEM) have improved detection limits and might soon become competitive, complementary methods to POSAP for analysis of these particles [11].

There is a fundamental problem with extracting quantitative compositional information from small-embedded particles because the matrix contributes to the signal. In our previous work we made an assumption that the particles were spherical in shape to overcome this difficulty and then described a procedure to confirm the assumption and allow measurement of the Fe content of the Cu-rich particles [12]. The largely spherical nature of the particles is well documented for thermally aged Fe–Cu alloys in the case of the larger (diameter > ~5 nm) particles which have transformed from their initial b.c.c. structure into a 9R structure that can be directly imaged using HREM [2, 13–15]. The smaller, un-transformed b.c.c. particles, however, cannot be directly imaged by HREM although the associated strain field can sometimes be seen using diffraction contrast methods [16]. It is the potential for using EFTEM for direct imaging of all the particles, both b.c.c. and transformed 9R, and for measuring their Fe content that is the subject of this paper.

The EFTEM imaging procedure requires the recording of at least two images of the same specimen area, using

S. Lozano-Perez (✉) · J. M. Titchmarsh · M. L. Jenkins
Department of Materials, University of Oxford, Parks Road, Oxford OX1 3PH, UK
e-mail: sergio.lozano-perez@materials.ox.ac.uk

energy windows below and one above the selected ionisation edge, to generate a jump-ratio image or a map with intensity proportional to the elemental concentration [17]. The spatial resolution and elemental sensitivity within an EFTEM image then depend on many factors including: composition of the sample, choice of ionisation edge, data acquisition time, energy window width, collection angle, sample thickness, the spherical, chromatic and diffraction aberrations, sample drift and spectrometer instabilities. These are well documented in the literature [18–30]. In previous publications, the experimental optimisation of some of these parameters has been described for EFTEM imaging of the Cu-rich precipitates [12, 31]. We also described the use of series of larger numbers (>3) of EFTEM images for generating the elemental maps. A fundamental issue is that, although the signal intensity and signal to noise can be improved by increasing parameters such as the acquisition time, number of images, energy window width and collection angle, these changes introduce additional image drift and correlation problems while degrading fundamental image resolution [18, 21, 23]. A conclusion from that work was that the sample drift could be measured from the image series and used to assess the degradation of both resolution and compositional accuracy. The modelling work described below follows from that observation, with a specific aim of correcting particle measurements for drift, fundamental resolution limits and signal to noise.

Experimental analysis procedures

The data acquisition and analysis procedures have already been described in detail elsewhere and only the major features will be summarised here [12].

Samples of Fe–Cu were heat-treated to nucleate a distribution of Cu-rich particles and later electro-polished for characterisation in a JEOL 2200FS TEM with an in-column filter operated at 200 keV accelerating voltage. EFTEM image series were recorded using specifically designed Digital Micrograph software scripts. Up to 40 images were recorded at 10 eV energy loss intervals using a 10 eV energy window width and a signal collection angle (β) of 12.1mrad within the energy-loss range between 640 eV and 1040 eV to include the Fe-L_{23} and Cu-L_{23} edges of interest. Further scripts allowed acquisition of image series with changing energy loss below the ionisation edge but repeated acquisition at a specific 10 eV energy window just above the edge. The position of the window was chosen to optimise the SNR, as described in [32]. This new feature enabled an improvement in the post-edge signal collected in any given time, compared with collecting the same number of post-edge images over a range of energy-loss values, because the maximum signal occurs close to the Fe-L_{23} and Cu-L_{23} edges. Foil thickness, t, maps were obtained from low-loss images using standard procedures [17]. Various acquisition times were compared.

Image correlation was achieved to an accuracy of one pixel (i.e. 0.1 to 0.3 nm, depending on image magnification) [33]. Displacements between consecutive images were used to estimate the degradation of image resolution by drift [12, 31]. Both Fe and Cu elemental maps were generated using various numbers of pre-edge maps fitted to a simple AE^{-r} power law.

The particles were revealed either as dark features on a brighter background (Cu-L_{23} image) or as bright features on a dark background (Fe-L_{23} image). A comparison of the signal-to-noise (SNR) and signal-to-background (SBR) ratios of the two corresponding maps is described later. Analysis of the shape of each particle was performed by comparing the measured intensity profile across the particle diameter with the corresponding theoretical profile for a spherical particle given by Eq. 1.

$$I = A + 2k\sqrt{R^2 - x^2 - y^2} \tag{1}$$

The particle, radius R, is centred at the origin of co-ordinates. A and k are scaling parameters. The intensity at all adjacent points in the matrix has a constant value provided the foil thickness is uniform. In the present investigation, any residual Cu in the Fe matrix had a concentration $\ll 1\%$ and could be ignored. Hence, for the Fe-L_{23} elemental map, A was the matrix intensity from a specimen of thickness t and the parameter k was equal to $-A/t$ if the precipitate contained no Fe. For the Cu-L_{23} maps, $A = 0$ and k had to be determined by separate calibration.

Confirmation of particle sphericity was made by fitting Eq. 1 to four profiles through the precipitate (at 45° rotations) using a maximum likelihood fitting procedure [34] to confirm that a constant radius value was obtained within experimental error. The reduction in intensity was then integrated over a square area containing the particle to determine a more accurate measurement of the sphere (i.e. using all the intensity loss rather than a small proportion along a diameter). It should be noted that local differences in thickness can limit the accuracy of this measurement. An annular integration area around the precipitate is suggested for future measurements. The line profile intensity minimum provided a measurement of the remaining Fe in the particle. When the profile width and depth simultaneously fitted Eq. 1 then the Fe content was zero. If the particle appeared to be circular (i.e. assumed to be spherical) but the experimental profile was shallower than predicted then

the Fe content was found by scaling the experimental and theoretical profiles. (NB The Fe map really shows the 'non-Fe' distribution rather than a Cu distribution, because other alloying and impurity elements can be incorporated into the particles. However, this does not affect the accuracy of the analysis of the Fe content.)

An alternative measurement of particle size was also derived from the full-width, half-maximum (FWHM) of the line profiles, although there is no simple relationship between the actual radius and the FWHM value.

The SNR for the Fe-L_{23} maps was measured as the ratio of the standard deviation of the pixel intensity at the fitted profile minimum to the average pixel intensity at the minimum; the SBR was measured from the average matrix intensity to the profile minimum intensity. For the Cu-L_{23} maps, the SNR was measured as the ratio of the standard deviation of the pixel intensity at the fitted profile maximum to the average pixel intensity at the maximum and the SBR from the profile maximum intensity to the matrix intensity.

Modelling procedures

In the ''traditional'' 3-window technique [17], two images are acquired before the edge and used to extrapolate the background to the energy of the single post-edge image. Although this method has some computational advantages when fitting to a power-law formula, especially if the windows are contiguous and have the same width, it still uses the minimum possible number of data points required to fit a curve, i.e. two. Accuracy can be poor when the images are noisy and solutions have been proposed to overcome this, such as the use of averaged fitting parameters or, when the background cannot be modelled with the traditional power-law, polynomial fits or maximum likelihood methods [35–37]. For all models there will still be an uncertainty in the extrapolation of the background [17, 18], but comparison of the absolute accuracy of different methods is not straightforward. The accuracy of background fitting is expected to improve as both the number of pre-edge data points and the SNR increase. Experimentally, however, both increase the total acquisition time and, therefore, drift.

In this project, a modelling investigation was undertaken to assess the accuracy and time-efficiency of strategies for background extrapolation that used different numbers of pre-edge windows containing different levels of noise. The modelling assumed a power law pre-edge continuum distribution, $a \cdot E^{-r}$, with a and r the fitting parameters, although any background shape could be used in principle, and that all the images were perfectly cross-correlated.

Once the background was artificially generated and scaled to a selected intensity, corresponding random (Poisson) noise was added to each energy bin (window) value in the 'spectrum'. Then, two or more fitting points, equally separated by $\Delta(E)$, were selected and a best-fit power-law curve calculated using the least-squares method. The best-fit power law was then used to extrapolate the value at a contiguous point $\Delta(E)$ in energy above the highest energy value used for fitting. Finally, the extrapolated value was compared with the original theoretical value at that energy and the relative error of the fitting measured. This procedure was repeated several hundred times until a smooth distribution of error against noise intensity was obtained. Results are described in the next section.

The effects of image drift, image blurring by fundamental electron optical limits and SNR were assessed by modelling the EFTEM appearance of particles over a wide range of these three variables. The radii of the modelled features were then determined by treating the results in the same manner as the experimental particle images, i.e. by fitting Eq. 1 to the modelled data using the same maximum likelihood algorithm and by measuring the FWHM.

In the previous report it was shown that, once the sample had been allowed to stabilise in the microscope, drift during the data recording was random and could be approximately quantified over many images by a normal distribution in two dimensions, with a magnitude related to the average displacement between successive images; such drift distorts each experimental circular image into an oval [12]. A theoretical Fe-L_{23} image was generated from Eq. 1 for a particle with a nominal diameter of 100 pixels, rather than an absolute value in nanometres. By defining drift and blurring amplitudes also in pixels, rather than absolute values, all generated results were then normalised for subsequent general application. A random number generator was then used to generate a magnitude and direction of drift and the corresponding distorted image calculated from the perfect image. This procedure was repeated with a different amplitude and direction and the intensity added to the first. By aggregating 100 such images, the average effect of blurring due to drift was calculated. This procedure was repeated for a range of drift distribution amplitudes between 0 and 150 pixels.

The resolution limit in an EFTEM map is determined by the diffraction limit (i.e. the accelerating voltage), the spherical and chromatic aberration coefficients of the objective lens, the signal collection half-angle, the width of the energy window and the energy loss and the 'de-localisation' of the signal [18–30]. A theoretical point source in the sample would be blurred by these parameters. The method of Krivanek [21], with the appropriate experimental and microscope parameters for the current investigation, was used to determine the magnitude of the blurring. Each pixel of the map, blurred by a specific drift

amplitude, was then treated as a point object and blurred by convolution with a 2-dimentional Gaussian distribution of width determined by a specified resolution limit. The convolutions were repeated for resolution values in the range 0–150 pixels for each of the aggregated drift amplitude images to generate a matrix of images blurred and 'drifted' by up to two times the particle diameter.

Each blurred, drifted image in the matrix was then degraded by the addition of an appropriate amount of random Poisson noise corresponding to a specified, mean signal intensity to simulate the effect of varying the data acquisition time and beam intensity. The noise at each pixel was generated using a random number generator. The whole procedure was repeated on each image in the 2-dimensional matrix for a range of SNR, to generate a 3-dimensional array of images.

Each of the images was then processed as though it was an experimental image to determine the FWHM diameter and the maximum likelihood estimate of the diameter. The difference between the true value (100 pixels) and these measured values were plotted against the three modelling variables.

Results

In Fig. 1, the systematic error in background extrapolation versus the noise level of the data is compared for three different methods each using windows of a constant energy width: (i) the conventional three-window method using two pre-edge windows for background fitting and an acquisition time t for each window, (ii) the same as (i) but doubling the time of acquisition and (iii) three pre-edge windows with acquisition time t.

It is seen that the use of only 2 pre-edge windows produces the worst extrapolation error. The effect of either doubling the acquisition time for the same two windows or including an extra pre-edge window with the same time, τ,

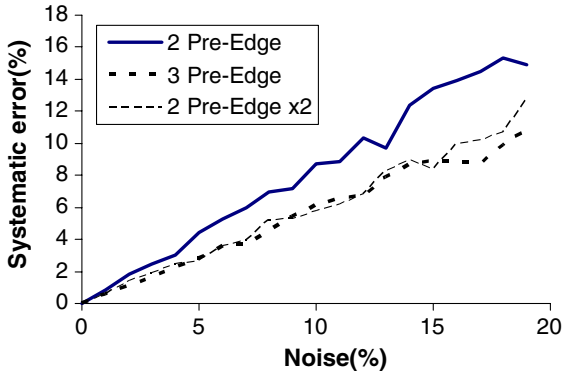

Fig. 1 Systematic error in the determination of the post-edge window background for 3 different methods

improves the accuracy of the fitting substantially and by similar amounts (Fig. 1). However, doubling the two pre-edge window acquisition time requires a total acquisition time of 4τ, while using 3 pre-edge windows only requires 3τ. Thus, it can be seen that the use of 3 pre-edge images is the most economic procedure. Based on this modelling, an assumption was made that, for a given total acquisition time and noise level, the greatest accuracy of background estimation would be achieved using several pre-edge images rather than just two. This strategy was use for the experimental results described below.

Cu (Fig. 2a) and Fe (Fig. 2b) elemental maps of the same area were used to assess which was the more suitable for composition measurement; i.e. which gave the better sensitivity for a given data acquisition time. Two consecutive 10 eV pre-edge windows were used for background subtraction. Several of the very large Fe-deficient (dark) features revealed in Fig. 2b.were not present in Fig. 2a and these were not the Cu-rich precipitates of interest. They were likely to be other types of precipitate often present in thermally aged ferritic steels, such as carbides. Intensity profiles along the diameter indicated for the round particle, bright in Fig. 2a and dark in Fig. 2b, are presented in Fig. 3. Superposed on the intensity profiles are the

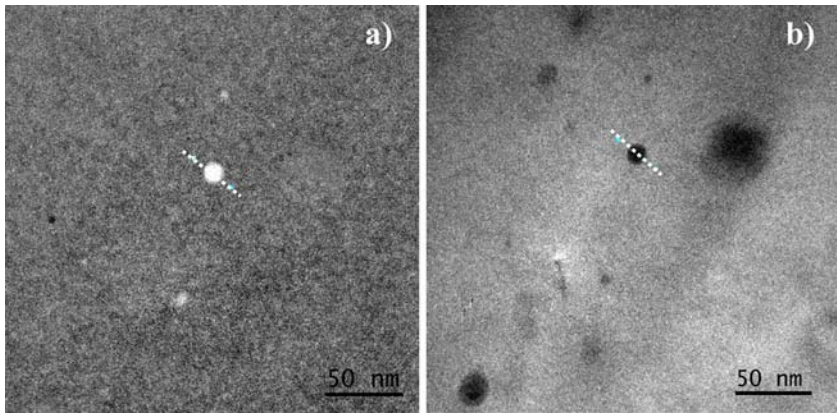

Fig. 2 (**a**) Cu-L_{23} and (**b**) Fe-L_{23} elemental maps of the same area of sample. The line through the largest particle in (**a**) indicates the location of the intensity profiles shown in Fig. 3

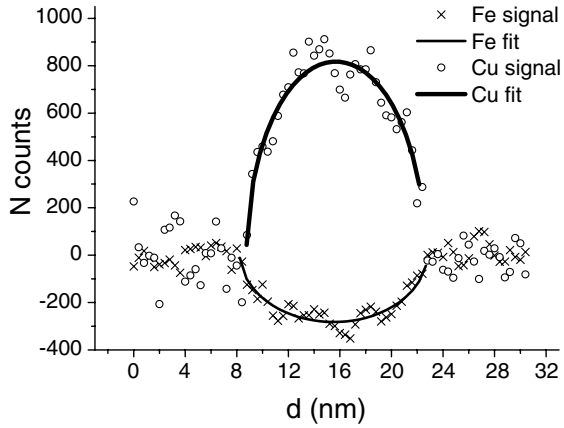

Fig. 3 Measured intensity profiles and maximum likelihood best fit curves along the particle diameter indicated in Fig. 2 for the Cu and Fe elemental signals

maximum likelihood (ML) best fits of the data to Eq. 1 and these were used to measure the SNR, as defined earlier. The acquisition parameters and the measured SNR are listed in Table 1. Although the SNR is very similar for the two maps, the Cu map was generated using longer data acquisition times (50 s per window compared with 20 s) and a larger energy window (40 eV compared with 10 eV) than the Fe map, thereby increasing drift and chromatic blurring. Hence, the use of the Fe deficit maps is to be preferred rather than the Cu maps. The thickness was measured using a t/λ thickness map [17] and found to be ~30 nm in this area. A 10% uncertainty is expected in this sort of measurements.

Having established that, for a given total acquisition time, the sensitivity would be optimised using Fe-L_{23} mapping together with background subtraction using multiple pre-edge windows, the detection limit for the Cu-rich particles was assessed. An initial characterisation of the drift revealed that it was random in direction and of approximately 0.1 nm in modulus for 20 s acquisitions. Under these conditions five 10 eV pre-edge images were acquired (660–710 eV) and ten 10 eV post-edge images, all at 720 eV. A 12mrad objective aperture was used with a beam current of ~29 nA. All the images were cross-correlated and aligned in the way described by Schaffer [33]. The 10 post-edge images were averaged to be compatible with the pre-edge images. A power-law curve was used to fit the background and the resultant Fe elemental map can be seen in Fig. 4.

In Fig. 4 there are several visible precipitates with sizes in the range 1.5–2.0 nm. The resolution was assessed from line profiles (Fig. 5) across the precipitates labelled 1 and

Table 1 Parameters used for the generation of maps in Fig. 2

	Fe-L_{23} map	Cu-L_{23} map
Energy loss window (eV)	720	920
Energy slit width (eV)	10	40
Collection half-angle (mrad)	12	12
Instrument blurring (nm)	0.7	1.2
Image acquisition time (seconds)	20	50
Number of pre-edge windows	2	2
Number of post edge images	1	1
Parameter k in Eq. 1	20	60
Standard error of channel counts	50	150
Noise % (SNR)	20 (5.0)	22 (4.6)

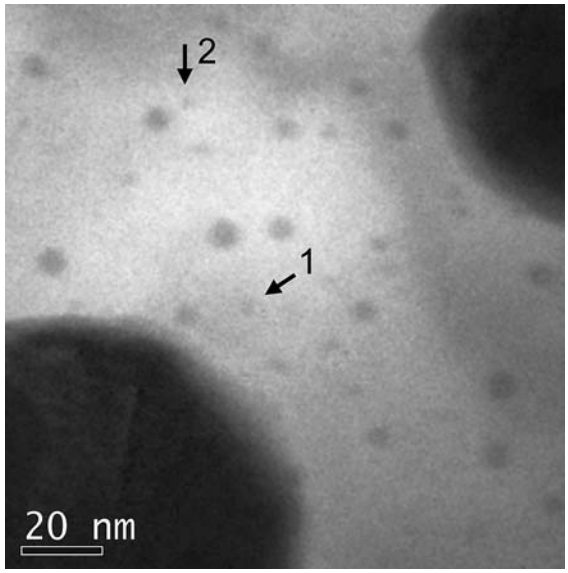

Fig. 4 Fe-L_{23} elemental map showing a distribution of Cu-rich particles with diameter <5 nm

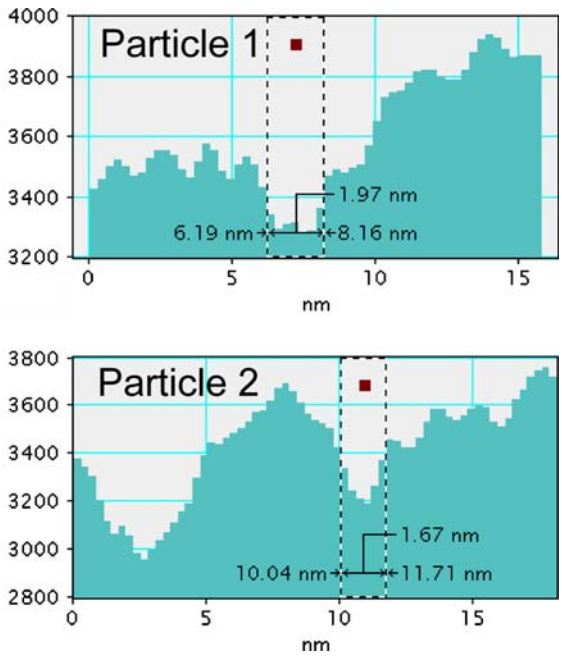

Fig. 5 Intensity line profiles through the two particles numbered in Fig. 4

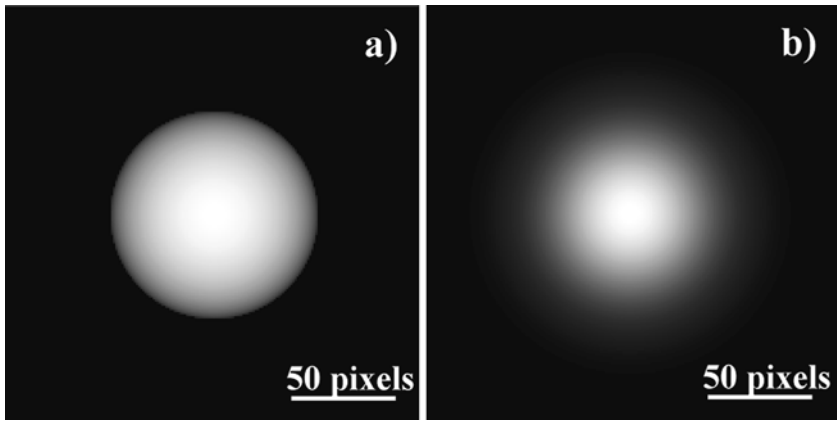

Fig. 6 (**a**) Ideal particle intensity calculated from Eq. 1 and (**b**) after instrumental blurring

2. Both show a FWHM diameter between 1.5 nm and 2.0 nm and a SNR = 4, close to the acceptable value for discrimination [38] and sufficient to attempt quantification of the Fe content [12]. The thickness was measured using a t/λ thickness map and found to be ~27 nm in this area However, the effects of drift and instrumental blurring, in addition to SNR, ideally require assessment and correction using the modelling results below.

The degradation of an ideal precipitate image in Fig. 6a, generated from Eq. 1, with a diameter of 100 pixels, after blurring by an instrument blurring parameter of 50 pixels is shown in Fig. 6b: the edge of the particle image is clearly smoothed under these conditions. Line profiles across a particle image after convolution with blurring functions of widths up to 100% of the 100-pixel particle diameter are shown in Fig. 7. The distortion of the same ideal particle image by drift with average magnitude equal to the particle radius during acquisition is shown in Fig. 8a. The superposed images of 100 such images, each with a drift amplitude randomly selected from a Gaussian distribution of 50 pixels FWHM, and with random direction, is shown in Fig. 8b. Figure 9 shows line profiles across a series of images generated with drift amplitude distributions up to 150% of the particle diameter (i.e.150 pixels).

The effect of adding random noise to an ideal image is illustrated in Fig. 10 which shows the expected result that, for a given average noise percentage of the maximum ideal intensity, the measured SNR increases as square-root of the number of summed images. This verified the integrity of the simulation algorithm.

The modelling results incorporating these three effects, in combination, are presented as 3-dimensional plots of the error in the radius determination against either the drift and image blurring with no noise (Fig. 11a and c), or noise and image blurring with zero drift (Fig. 11b and d). In Fig. 11a and b the radius was determined by maximum likelihood (ML) fitting to line profiles across the simulated images, while in Fig. 11c and d the FWHM radius values were

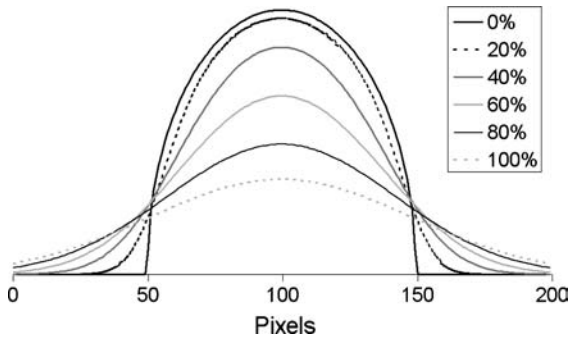

Fig. 7 Modelled intensity profiles showing the increased blurring as the instrument blurring parameter increases

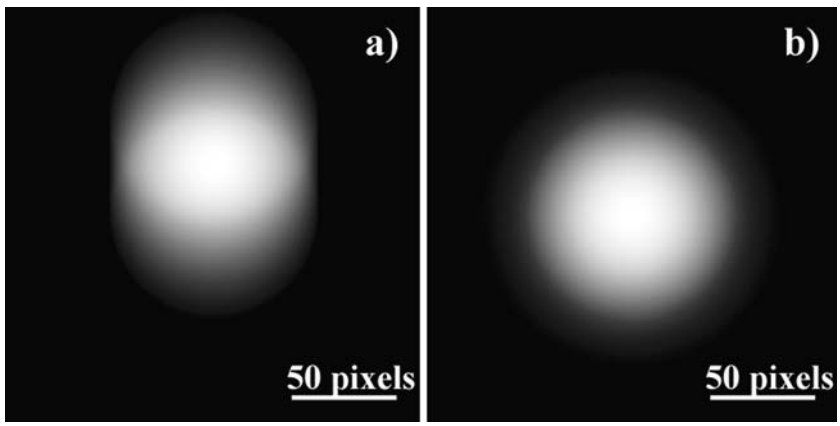

Fig. 8 (**a**) Modelled particle intensity map, assuming a uniform linear drift during acquisition and (**b**) superposition of 100 maps with random drift directions from a single amplitude distribution

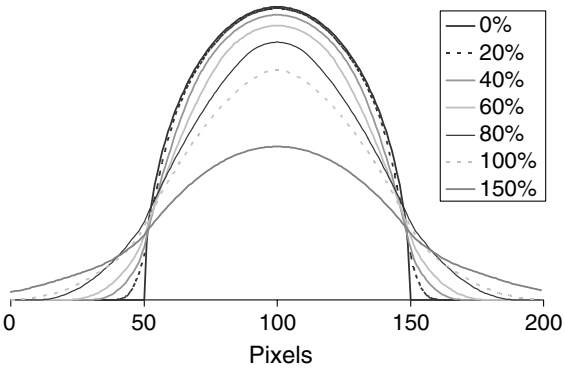

Fig. 9 Intensity profiles through a series of images such as that in Fig. 8b as the amplitude increases

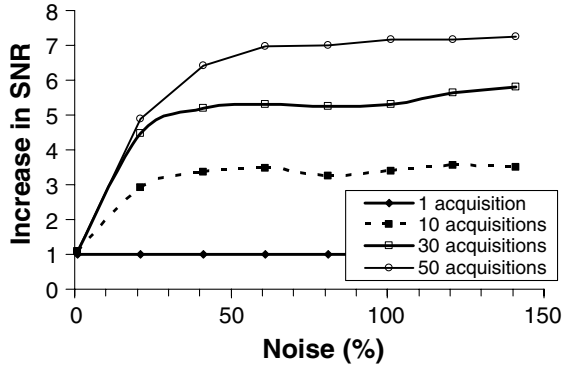

Fig. 10 Variation of SNR as a function of the absolute noise magnitude as the number of aggregated acquisitions increases

determined from the same set of images. The major observations to be made from these results are discussed below.

Discussion

The modelling results from the previous section suggest that, when the size of the particle is of the same order as the average drift or the instrument blurring, large imaging artefacts can occur. It is clear that alternative measurement methods of the particle radius might lead to different results. In particular, when the FWHM is used there is a range of drift and blur values ($0 < \text{drift} < 110\%$ and $0 < \text{blur} < 60\%$) for which the measured particle radius is smaller than the actual value (Fig. 12). This occurs because the image degradation blurs the edges of the particle image but does not reduce the central intensity significantly when the particle radius is much greater than the instrument blurring parameter. The effect of larger parameter values is always to enlarge the measured FWHM size, as one would intuitively expect. The measured ML radius is always larger than the actual radius except when the image is very noisy, when occasional negative values are possible.

It is also observed that the separate combination of noise with the other two variables is different. In Fig. 11b it is seen how, in the absence of drift and blurring, the ML best-fit radius resists perfectly noise levels up to 100% of the signal intensity, while the FWHM has an error of up to 2% when the noise is higher than 80%. The ML least squares fitting method is much more effective than the FWHM method for minimising the effects of random noise (note the difference in error scales in Fig. 11b and d). Even when the SNR ~ 0.33 (noise = 300%, Fig. 11b) the error in radius is minimal when the instrumental blurring is small using ML, whereas the FWHM values become very variable. Therefore, the use of the ML least-squares method to determine the size of the particle is recommended.

The smooth error surface which is generated with zero noise is more sensitive to instrumental blurring than drift (Fig. 11a and c). This probably occurs because the elongation of the image in the drift direction is compensated by a narrowing of the distribution of image intensity (i.e. image sharpening) normal to the drift direction (Fig. 8). The overall blurring effect of drift, therefore, is partly compensated when many randomly drifted images are superposed, whereas instrumental blurring is always present equally in all directions. Surfaces equivalent to those shown in Fig. 11a and c, but corresponding to non-zero levels of noise, can be generated for any specific, measured SNR value. This provides the potential for correction, or partial correction, of ML radius measurements for drift and blurring. The correction procedure would have to be iterative because the actual particle radius is unknown, so initial values of normalised drift and blur parameters would be estimated from the measured radius, drift and relevant instrument blur value. Correction would lead to a better estimate of the radius, leading to modified, more accurate normalised drift and blur values. Further iterations could be applied, as required.

The measurement accuracy of the Fe content of a particle depends on the difference between the ideal profile, described by Eq. 1, and the minimum depth measured for a specific measured radius. As the blurring increases relative to the true particle radius, the profile minimum from a 0%Fe-particle will become shallower. The difference between the blurred and ideal minima is plotted in Fig. 11e and f as the percentage error in Fe content as a function of both noise and instrumental blur (Fig. 11f) and drift and instrumental blur (Fig. 11e). It is observed that the noise has little effect on the apparent Fe content until its magnitude is similar to the signal intensity. The instrumental blurring has a very significant effect, however, while the drift has an intermediate influence. These observations are seen more clearly in Fig. 12 where the variation of the

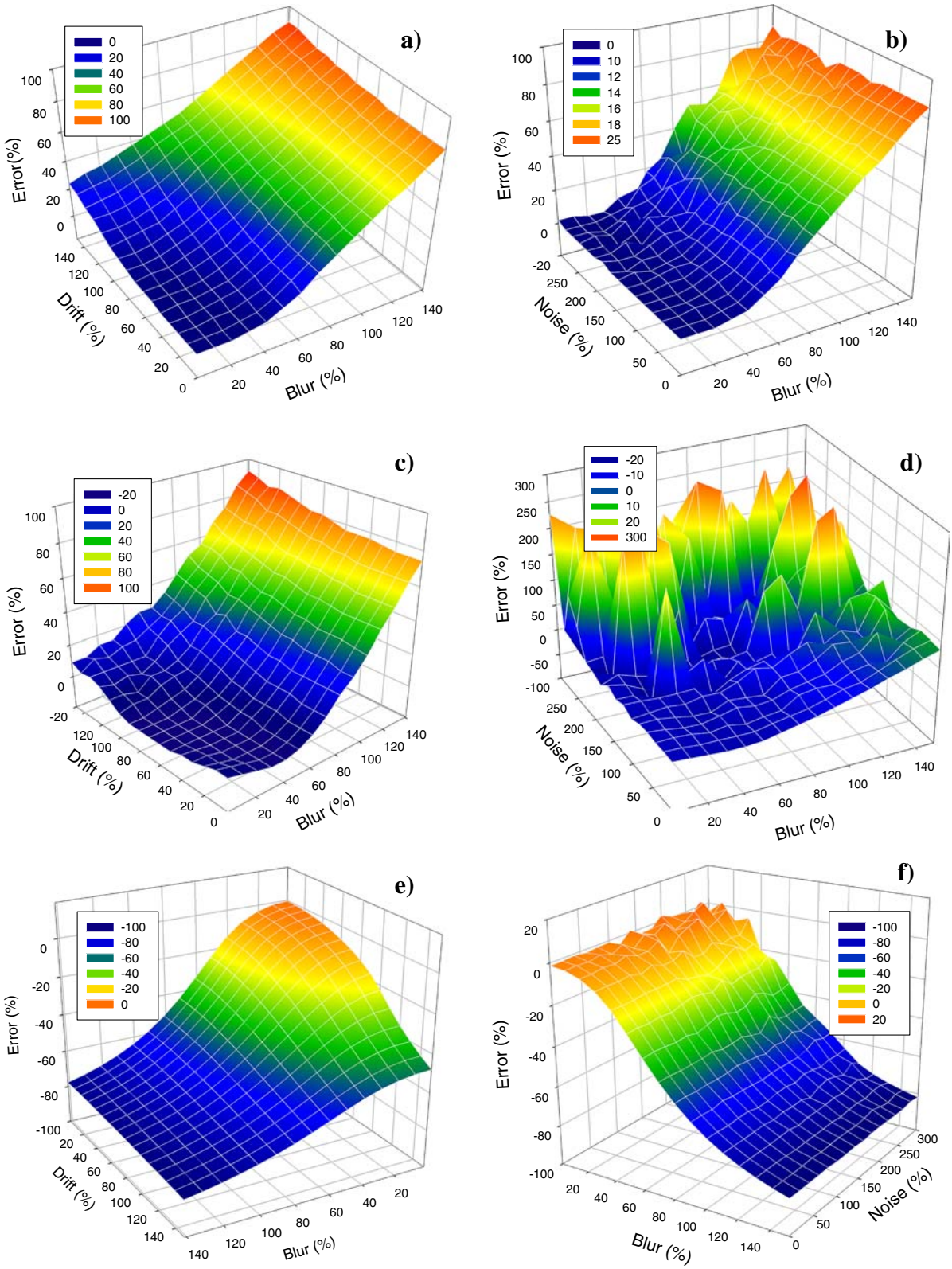

Fig. 11 Percentage error in ML determination of particle radius as a function of (**a**) drift and instrumental blur and (**b**) noise and instrumental blur. Percentage error in FWHM determination of particle radius as a function of: (**c**) drift and instrumental blur and (**d**) noise and instrumental blur. Error in measured Fe content of precipitates as a function of (**a**) drift and instrumental blur and (**b**) instrumental blur and noise. Positive values mean overestimation and negative underestimation

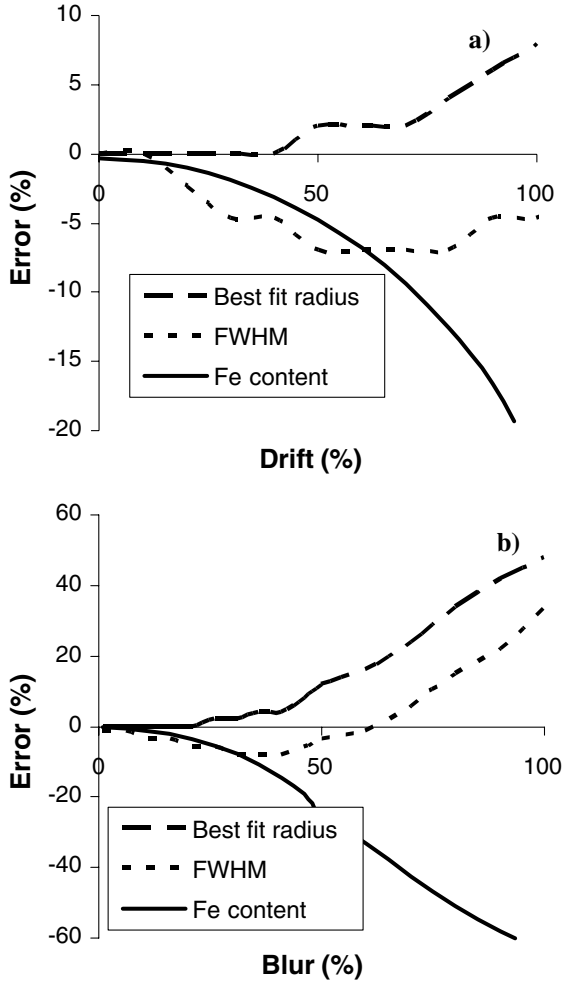

Fig. 12 (**a**) Comparison of errors in ML radius, FWHM radius and Fe content for drift, with no blur or noise; (**b**) Comparison of errors in ML radius, FWHM radius and Fe content for blur with no drift or noise

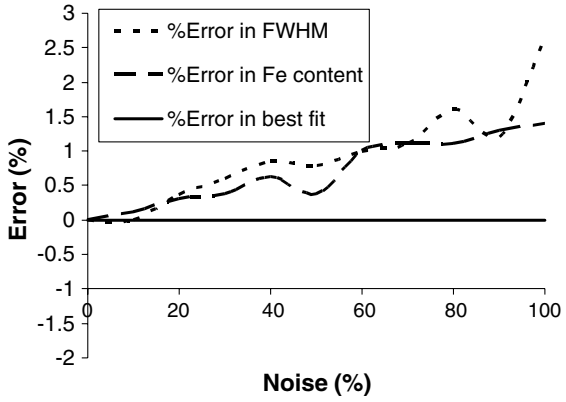

Fig. 13 Comparison of systematic measurement errors in ML radius, FWHM radius and Fe content for different levels of noise

error in Fe content is plotted separately for the three parameters: for each variable parameter the value of the other two parameters is zero. As discussed in [12], thickness determination is a key issue. The uncertainty in the thickness determination will ultimately compromise the accuracy of any Fe concentration calculations. Thickness will also have a detrimental effect on the elemental map SNR when it becomes comparable or bigger than the inelastic mean free path, as stated in [17, 18]. The systematic percentage error in the estimation of the precipitate size using ML and FWHM, as well as in the Fe content, are shown for reference in Fig. 13.

The radius can be measured more accurately and independent of the line profile [12] by calculating the size of a sphere that produces the integrated Fe intensity reduction over the whole particle. When this integrated radius measurement, r_I, is the same as that from the ML line profile, r_{LP}, then the particle should contain no Fe. However, differences will occur when either (i) the particle contains significant Fe or (ii) the r_{LP} has been blurred, or both. It becomes more difficult to discriminate between these two possibilities as the precipitate radius decreases. In principle, however, the magnitude of blurring can now be modelled and the two situations discriminated. A correction for the error in Cu-content can be estimated from the ML best fit radius and surfaces such as those in Fig. 12b for the appropriate drift, noise and blur. Any remaining difference between the measured profile minimum and the profile minimum corrected for artefacts will be due to the presence of Fe in the particle.

The ML radii measured in Fig. 4 were 0.84 and 0.99 nm, with drift of only 0.1 nm (~12% and 10%, respectively), blurring of ~0.7 nm (83% and 70%, respectively) and a SNR~4 (corresponding to noise of 25%). Referencing the previous results (Figs. 11 and 13), the blurring will cause by far the greatest error in the measurement of the ML radius. When the effect of any noise and drift is ignored, ML radius correction factors of ~15% and ~10%, respectively, can be derived from Fig. 13, resulting in better estimates of 0.73 nm and 0.90 nm, respectively, for the radii of the two particles.

As already noted, there are two methods by which the particle radius can be measured from the maps: (i) from the ML least squares calculation where the radius, r_{LP}, is systematically varied until the optimum fit is determined or (ii) r_I, from the difference between the integrated Fe intensity in equally-sized boxes containing the particle and the matrix. The latter is more accurate because it is unaffected by blurring and drift. In Fig. 14 a range of experimentally measured r_I values are plotted against the corresponding ML r_{LP} values for the same group of particles. The data acquisition parameters are listed in Table 2. Ideally, all points should lie on the line of unit gradient. Corrections to the r_{LP} values were derived using the modelling illustrated in Figs. 11 and 12b and the corrected values are also plotted in Fig. 14. As, expected, the

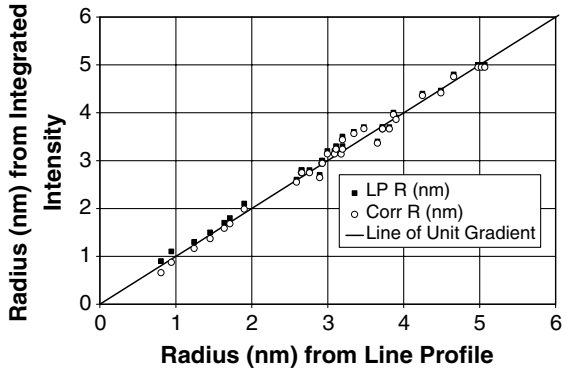

Fig. 14 Comparison of corrected and uncorrected values of the ML radius for a range of particle radii

Table 2 Parameters for the data acquisition of Fe-L23 maps used to generate Fig. 4

Energy loss window (eV)	720
Energy slit width (eV)	10
Collection half-angle (mrad)	12
Instrument blurring (nm)	0.7
Image acquisition time (seconds)	20
Number of pre-edge windows	5
Number of post edge images	10
Noise % (SNR)	7 (14)
Average drift per image (nm)	0.4
Instrument blurring (nm)	0.7

corrected values always lie below the measured values and the relative difference increases as the radius decreases. Both data sets generally follow the line of unit gradient although there is some scatter in the radius range above 2.5 nm. The reason for this is uncertain because the accuracy of fit should improve with increasing radius. However, the particles could become more facetted as they grow, or the larger particles might be those that have transformed from the b.c.c. structure to the 9R phase and begun to exhibit some faceting. Both the radius distributions below 2.5 nm closely follow the unit gradient line but the uncorrected values tend to lie slightly above the line while the corrected values lie slightly below but closer to the line. Hence, there seems to be a small benefit to be gained from correction. However, the relatively small correction factors calculated for this data set suggest that it should be possible to analyse even smaller particles by increasing data acquisition times, even though this increases drift, and/or even by using larger energy windows, even though this increases instrumental blur, because correction is feasible.

Conclusions

It is possible to measure the radius and chemical composition of small Cu-rich particles embedded in a ferritic (Fe) matrix using EFTEM. Greater measurement accuracy is achieved by dividing a given analysis time to acquire several pre-edge background fitting windows rather than to divide the time for just two pre-edge windows. It is feasible to determine appropriate factors to correct the degrading influence of noise, drift and instrumental blurring. It is experimentally possible to reveal particles with radii less than one nanometre and to correct such small measured radii, improving the accuracy of residual Fe (Cu) concentration measurements.

Acknowledgements We thank the EPSRC, Rolls Royce and the Institute of Nuclear Safety System (INSS), Japan, for support for this work. JMT was further supported by the Royal Academy of Engineering, BNFL and INSS.

References

1. Barashev AV, Golubov SI, Bacon DJ, Flewitt PEJ, Lewis TA (2004) Acta Mate 52:877
2. Othen PJ, Jenkins ML, Smith GDW, Phythian WJ (1991) Phil Mag Lett 64:383
3. Lucas GE, Odette GR, Maiti R, Sheckherd JW (1987) 13th International Symposium on Influence of Radiation on Materials Properties, p 379
4. Carter RG, Soneda N, Dohi K, Hyde JM, English CA, Server WL (2001) J Nucl Mater 298:211
5. Miller MK, Wirth BD, Odette GR (2003) Mater Sci Eng A-Structural Materials Properties Microstructure and Processing 353:133
6. Vaumousse D, Cerezo A, Warren PJ (2003) Ultramicroscopy 95:215
7. Ishino S, Chimi Y, Bagiyono, Tobita T, Ishikawa N, Suzuki M, Iwase A (2003) J Nucl Mater 323:354
8. Scott PM (2000) Corrosion 56:771
9. Watanabe M, Williams D (2005) Microsc Microanal 11:1362
10. Yaguchi T, Konno M, Kamino T, Kaji K, Ohnishi T, Watanabe M (2005) Microsc Microanal 11:630
11. Lozano-Perez S, Sha G, Titchmarsh JM, Jenkins ML, Hirosawa S, Cerezo A, Smith GDW (2006) J. Mater. Sci. in press
12. Lozano-Perez S, Titchmarsh JM, Jenkins ML (2006) Ultramicroscopy 106:75
13. Monzen R, Iguchi M, Jenkins ML (2000) Phil Mag Lett 80:137
14. Othen PJ, Jenkins ML, Smith GDW (1994) Phil Mag A 70:1
15. Othen PJ (1992) Thesis, University of Oxford
16. Fonda RW, Cassada WA, Shiflet GJ (1992) Acta Metall Mater 40:2539
17. Egerton RF (1986) Electron energy-loss spectroscopy in the electron microscope. Plenum, New York
18. Berger A, Kohl H (1993) Optik 92:175
19. Kohl H, Berger A (1995) Ultramicroscopy 59:191
20. Egerton RF, Wong K (1995) Ultramicroscopy 59:169
21. Krivanek OL, Kundmann MK, Kimoto K (1995) J Microsc 180:277
22. Muller DA, Silcox J (1995) Ultramicroscopy 59:195
23. Egerton RF, Crozier PA (1997) Micron 28:117
24. Golla U, Kohl H (1997) Micron 28:397
25. Freitag B, Mader W (1999) J Microsc 194:42
26. Hofer F, Grogger W, Kothleitner G, Warbichler P (1999) Inst Phys Conf Ser EMAG 1999 161:169
27. Thomas PJ, Midgley PA (2001) Ultramicroscopy 88:179
28. Grogger W, Schaffer B, Krishnan KM, Hofer F (2003) Ultramicroscopy 96:481

29. Kothleitner G, Hofer F (2003) Ultramicroscopy 96:491
30. Watanabe M, Williams DB, Tomokiyo Y (2003) Micron 34:173
31. Lozano-Perez S, Jenkins MJ, Titchmarsh JM (2005) Microsc Microanal 11:486
32. Kothleitner G, Hofer F (1998) Micron 29:349
33. Schaffer B, Grogger W, Kothleitner G (2004) Ultramicroscopy 102:27
34. Mor JJ (1977) In: Watson GA (ed) Lecture Notes in Mathematics, Springer-Verlag, Berlin, p 105
35. Grogger W, Varela M, Ristau R, Schaffer B, Hofer F, Krishnan KM (2004) J Electron Spectrosc Related Phenom 143:141
36. Unser M, Ellis JR, Pun T, Eden M (1987) J Microsc 145:245
37. Egerton RF, Malac M (2002) Ultramicroscopy 92:47
38. Rose A (1970) Image Technol 12:13